Nuclear Engineering and Technology 58 (2026) 104048

Contents lists available at ScienceDirect

Nuclear Engineering and Technology

journal homepage: www.elsevier.com/locate/net

Original Article

Weldability of additive manufactured pipe features for fusion component replacement

Yao Ren *, Robert Skilton, Ian Merrigan, Neil Mayfield

UK Atomic Energy Authority Campus, Culham, Abingdon, OX14 3DB, UK

ARTICLE INFO

Keywords:
Nuclear fusion
Additive manufacturing
TIG welding
Cooling pipe
Remote maintenance

ABSTRACT

The current strategy for joining ITER divertor cooling pipes is to conduct semi-automated autogenous Tungsten Inert Gas (TIG) welding on thin-walled pipes using an inserted flat washer filler ring. In this approach, the positioning of the filler ring and the alignment of the pipe stubs so far can only be achieved manually. However, it has limitations for future maintenance because human interventions may be limited or completely prohibited in contaminated environments, requiring the need for remotely operated tools and systems. In addition, maintenance of cooling pipes will involve cutting and re-welding of the parts. However, components have limited lifespan for reuse. Additive manufacturing (AM) is an advanced technique that provides one potential way to overcome the limitations. This work investigates the use of the AM method to deposit material as an alternative approach to using filler rings, which a flange feature was firstly built on the pipe end using laser blown powder direct energy deposition (DED). Thereafter, semi-automated autogenous TIG welding was conducted on the AM modified pipe stubs. The results suggest that using the AM produced parts has achieved compliant pipe joins, implying possible improvements to maintenance strategies for future fusion power plants and experimental devices.

1. Background and objectives

1.1. Additive manufacturing applications in nuclear fusion

Fusion power is a proposed form of sustainable power generation that would generate electricity by using the heat from nuclear fusion reactions. Tokamak is a fusion machine in which plasma is driven by magnetic confined torus, and fusion reactions take place between the nuclei of the two heavy isotopes of hydrogen – deuterium (D) and tritium (T): $d + t \rightarrow {}^{4}He\ (3.5\ MeV) + n\ (14.1\ MeV)$ [1,2]. At the core of a fusion reactor, the temperature of the plasma is in excess of 150 million degrees Celsius. Although the plasma is actively held away from the walls of the tokamak by using powerful magnetic fields, small amounts of plasma still touch the walls. This results in a requirement on the inner wall material to withstand the impact of plasma touchdown without getting seriously damaged. D-T reaction generates high-energy neutrons, lack electric charge, that escape from the plasma and deposit their energy on the surrounding "blanket" components, which contain lithium in the breeding zone for the purpose of generating more tritium as further fuel for the reactor. The heat generated in the lithium blanket, as a result of the absorption of the kinetic energy from neutrons, will be collected for electricity generation through the embedded cooling systems [1,3].

It is challenging to develop advanced materials and manufacturing routes for critical components for fusion devices [4]. These components, such as plasma facing components (PFCs), breeding blankets, structures and ports, radiation and thermal shields, vacuum vessels, and magnets, may possess complex geometries, large dimensions, heavy weights, specifically designed functions, and multi-material interfaces. Materials used for manufacturing these components must not only accommodate advanced design requirements but also achieve operational performance in extreme environments [5]. For instance, the raw materials selected and their fabrication into structural components that are suitable for the environmental conditions, depend on adequate mechanical and thermos-physical properties, their behaviour under irradiation and the compatibility with other materials and cooling media, radiological properties, i.e. activity, decay heat, radiotoxicity [6]. The properties of the materials and components are also critically dependent on the manufacturing processes.

Additive manufacturing (AM) provides a highly promising path for

* Corresponding author.
E-mail address: yao.ren@ukaea.uk (Y. Ren).

https://doi.org/10.1016/j.net.2025.104048
Received 13 August 2025; Received in revised form 4 November 2025; Accepted 24 November 2025
Available online 27 November 2025

affordable fabrication of complex components in one-step [7–10]. ASTM F42 categorizes seven major AM processes, among which metal components and structures may be manufactured by powder-bed system, powder-feed system and wire-feed system, using laser beam, electron beam and electric arc as heating sources, through direct deposition, selective melting or sintering processes, under an inert gas atmosphere or vacuum condition [10–12]. AM has shown great potential for the development of fabrication routes towards realisation of nuclear critical structural components. Fabrication of ITER first wall panel parts, made of stainless steel 316, has been achieved using both selective laser melting (SLM) and electron beam melting (EBM) technologies, without cracks observed on the cross-section plane perpendicular to the building direction [10]. SLM manufactured EUROFER 97, without further treatment, possessed a unique bimodal microstructure of both untempered martensite as well as large ferrite grains elongated in build direction, which could lead to advantageous tensile properties in the form of higher flow stress and high uniform elongation, but also to an inferior impact toughness in comparison to conventional EUROFER97 [8]. Laser power bed fusion (PBF, here refers to SLM) and metal powder application (MPA) in combination with machining have demonstrated potential for the realisation of DEMO first wall, especially with regard the possibility to implement surface profiles, such as cooling plate with internal cooling channels, for heat transfer enhancement [9,13]. Laser metal deposition (LMD) is the process where the metallic powder or wire is fed into the laser spot through a nozzle, a 3D geometry then to be realised by moving the laser head or the part. This direct metal deposition process has been investigated to manufacture Reduced Activation Ferritic Martensitic (RAFM) steel and ODS EUROFER97 [14,15].

Some of the major concerns of using AM processes for fabrication of PFCs using refractory materials, such as Tungsten (W) using a laser or electron beam, include the high power required and the residual stresses generated through melting [16]. The DED of pure tungsten has shown decreased dilution with the increase of the thickness while W content built up, and the highest W content exited at the top of the part [17]. Wire Arc Additive Manufacturing (WAAM) has proven capable of producing fully dense large-scale W parts at relatively low cost, by using high-quality wire as feedstock [18]. Studies on SLM manufacturing of pure tungsten have focused on the factors, i.e. process parameters, powder morphology, as well as using pre-heated substrate, that affect the final material properties [19–21]. Electron beam powder bed fusion (EB-PBF) has shown promise in manufacturing pure tungsten via high thermal energy input, elevated build temperature, and a tightly controlled high-vacuum environment [22,23]. However, the wire-based EB process has achieved higher density compared to powder processes [24].

1.2. Additive manufacturing potential in fusion device maintenance

Cold spraying is considered as one of the emerging AM technologies [25–27]. It has been studied to produce metallic coating to obtain enhanced properties on different components, such as surface chemistry and wettability control, improved mechanical properties and anti-corrosive properties etc. It presents an advantageous potential of being able to apply coating directly onto the first wall surface, without subsequent welding or post-heat treatment [28,29].

Cladding, also called laser overlay welding [30], can be applied using laser DED technology. Unlike cold spraying, which is a mechanical bonding process, cladding creates a metallurgical bond between a metal substrate and a metal coating, providing protection to the metallic component from corrosion and wear. An example the application is to deposit hard-facing materials on the inner surface of diagrid tubes [31]. It also can be used for restoring and re-manufacturing high-value components into their original geometry. Service life and performance of the components can also be improved by selecting an additive material with better wear characteristics than the original component [32].

AM manufactured SS316L vie laser PBF has shown lower corrosion susceptibility than that of wrought 316L. It was also successfully welded to its counterpart under corrosion distress and retained more than 80 % of its yield and ultimate strength, which indicates a potential to use AM to replace broken legacy stainless steel pipeline assets, to reduce downtime and cost associated with its repair in relative industries [33]. In addition, AM equipment, tools and technical solutions are getting more compact, precise, versatile, and cheaper. By producing highly satisfactory, functionally graded, and smart structures whilst reducing production time, it makes AM the perfect technology for multi-material micro and macro in-situ repairs, including for remote maintenance in fusion devices [34,35].

Maintenance of pressurized water-cooling pipes in fusion devices requires operations using fully automated remote handling tools and systems. ITER divertor cooling pipes, made of stainless steel 316L, are to be remotely cut and re-welded during tokamak maintenance for the replacement of the divertor cassettes [36]. An autogenous orbital TIG welding process was adopted as it could avoid the risk of wire stuck on the workpiece due to potential failure of the wire feed mechanism, which however, limited the maximum pipe wall thickness to less than 3 mm [36–38], in order to achieve weld compliance with the French nuclear standard RCC-MRx.

Inspired by consumable inserts, pre-placed filler metal rings or strips that fused during pipe welding to aid fit-up and fuse the root pass, a flat washer insert filler ring was employed to accommodate the misalignment when fabricating ITER divertor cooling pipes [36]. Because the dimensions required for the filler ring were not commercially available, nor was it economically viable to manufacture a consumable with desired alloying elements, the filler ring, in thickness of 0.7 mm, was extracted from a slightly thicker-walled pipe but possessed identical chemical contents. Prior to the welding, the filler ring was first resistively spot welded onto the square-edged pipe stub end, allowing the following butt-welding process to be fully autogenous. The slightly proud edges on both sides of the pipe wall also guaranteed the achievement of qualified weld cap reinforcement and root penetration.

Although the goal for re-welding the pipes during reactor maintenance is to conduct fully automated operations, the TIG welding process developed for divertor pipe commissioning remained semi-automated, and human intervention was highly required during the setups. Especially when spot welding the filler ring, purge gas supply at the joining locations as well as the component fit-up was constantly monitored by the operator in case oxidation was introduced at the mating surfaces, which had the risk of leading to entrapment of pores during the subsequent welding.

1.3. Objectives and approach of this work

To increase the potential for automation of the welding set-up and preparation, this study proposes a concept of using laser powder DED to additively manufacture a small flange feature at the end of the pipe stub. Thereafter, machining the flange to the dimensions equivalent to the spot-welded filler ring and then butt joining this AM modified pipe stub to another pipe stub using a semi-automated autogenous orbital TIG process. The process parameters and welding procedures were developed based on the previous project, and the pipe material used was 316L stainless steel with a minimum of Sulphur (S) content of 0.008 % [36]. At about such a percentage of S or greater, the temperature coefficient of surface tension is positive, which means the area under the arc has the highest surface tension and the edges of the weld pool have lower surface tension. Such surface tension gradient causes the fluid of the weld pool to flow from the edges toward the centre, which is beneficial to achieving a narrow and deep weld. This is also known as the Marangoni effect. Equipment used for welding trials comprised a commercial orbital welding tool, a bespoke welding fixturing, and an ESAB power supply and a control package. Weld qualities were assessed by destructive and non-destructive testing. Results were also compared with the reference welds manufactured using the inserted filler ring. The

main objective of the work was to investigate the feasibility and weldability of a partially additively manufactured feature for nuclear graded piping, exploring the potentials of using AM for component modification and future maintenance for the use in fusion devices.

2. Materials and methodology

The components used in this research include 316L stainless steel pipes, 316L stainless steel insert filler ring and stainless steel 316L powder. The pipe material is grade 316L stainless steel with the S content at 0.01 % which is in the range of the Marangoni transition zone, but also not too high to induce solidification cracking [36]. The insert filler ring was extracted from a slightly thicker-walled pipe which comprised the identical chemical composition. The powder feedstock used was a commercially available stainless-steel grade 316L. The powder size is 20–53 μm. The main chemical compositions of both materials, provided by the suppliers, are listed in Table 1.

In this study, a laser powder DED manufacturing technique was explored to modify the end of the pipe stub, to mimic the geometry and function of the filler ring that was used in the autogenous welding of the ITER divertor cooling pipes [36]. The welding process and weld quality assessment are reported in Section 4. A semi-automated autogenous orbital TIG welding process was developed, with a corresponding preliminary Welding Procedure Specification (pWPS), to fabricate 12 welded pipe assemblies. There were six welds produced using the insert filler ring and six welds were produced from the AM modified feature. Developed welding process parameters are detailed in Section 4.1.

The quality of the welds was assessed through a series of non-destructive and destructive testing. Visual inspection and X-ray radiography were performed on all 12 fabricated welds (Section 4.2) before carrying out mechanical testing, and transverse macro cross-sectioning and metallography on the welds that have passed the non-destructive evaluation (NDE) (Section 4.3). Further investigations of the microstructural characterization and compositional analysis were conducted on three representative weld samples; one had AM modified feature, one was produced from the insert filler ring, and one experienced distinguished thermal history from re-welding processes, is summarized in Section 4.4.

3. Laser powder DED manufacturing

3.1. Component preparation and design

The first phase of this work was to deposit material onto the pipe ends in a manner that replicated the material that would be present when using filler rings. This was achieved using a Laser Powder DED method. Pipe samples were machined to size at the end where deposition takes place. The outer machined diameter of the pipe is nominally 70 mm and with a wall thickness of 2.7 mm. The length of the pipes was approximately 200 mm. The machined pipe end was shot blasted to dull the surface prior to the deposition, aiming to reduce the reflection of the incident laser beam. Fig. 1 shows a schematic drawing of the pipe and the deposited flange feature which had a minimum 2 mm overhang on both sides of the pipe wall and a minimum top coating thickness of 1.5 mm, to give sufficient post-machining tolerance. This machining tolerance was considered to give a safety margin and was chosen by taking into account surface undulations which might arise in the deposited material, and any movement of the pipe end due to thermally induced distortion.

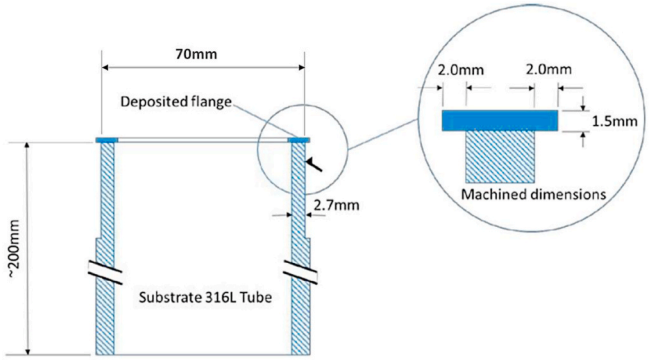

Fig. 1. Schematic diagram of pipe substrate and dimensions of the deposited flange.

3.2. Equipment and setup

Process development was carried out using a Trumpf DMD 505 laser deposition system which comprised three sub system: a Fraunhofer ILT 40 mm coaxial powder feed nozzle with a stand-off set to 11 mm, a Sulzer Metco dual hopper 10-C powder feeder with 1.5 L capacity per hopper and a temperature-controlled heating jacket, and a manipulation of the nozzle (in x, y, z directions) and CNC table (rotation and tilt). The power source used was a Trumpf 1.8 kW HQ CO2 laser. The laser exhibited a Gaussian energy distribution across the focused beam. During the deposition, the laser processing head was positioned in a top-down configuration at a fixed stand-off distance to the material's upper surface. Argon gas was distributed through a Cryospeed system for a shielding purpose and for use as a powder carrier gas.

3.3. Process development

The build methodology and toolpath approach to manufacturing the flanges were split into three steps: the internal flange, the external flange, and the top coating (Fig. 2). Each step employed a spiralling toolpath, with a pitch equal to the scan spacing or layer height, which was achieved by simultaneous and synchronous movement of the pipe rotation and nozzle traverse. To build the internal flange, the pipe was tilted to 31° at the start of this step to provide suitable nozzle access to the deposition surface. The pipe was rotated, and the nozzle was incremented in both the -X and +Z directions to build a wall using a spiralling toolpath, forming a wall perpendicular to the pipe surface. The speed of the nozzle and the revolutions per minute (rpm) of the pipe were calculated to give an equivalent nozzle transverse speed of 600 mm/min.

The building of the external flange was achieved by rotating the pipe axis to a horizontal position and the cladding nozzle was positioned above the top surface of the pipe. During the deposition, the pipe was rotated, and the nozzle was incremented in the +Z direction (See Fig. 2) to form a wall which was perpendicular to the pipe wall. For both the internal and external wall builds, a single pass melt bead was employed which gave a nominal wall thickness of 1.5 mm, similar in width to the width of the melt pool/track.

On completion of the external flange, the pipe axis was then oriented into a vertical position and the coating layer was produced across the entire area of the flanges and the pipe end. The coating was applied using a spiralling toolpath. The nozzle was positioned at the outside

Table 1
Material chemical composition for both the pipe and powder feedstock used.

Chemical Composition %	C	Cr	Si	P	S	Ni	Mn	Mo	N
316L Pipe	0.0230	16.760	0.310	0.039	0.010	10.080	1.640	2.030	0.064
316L powder	0.0160	17.100	0.700	–	–	12.400	1.500	2.600	0.100

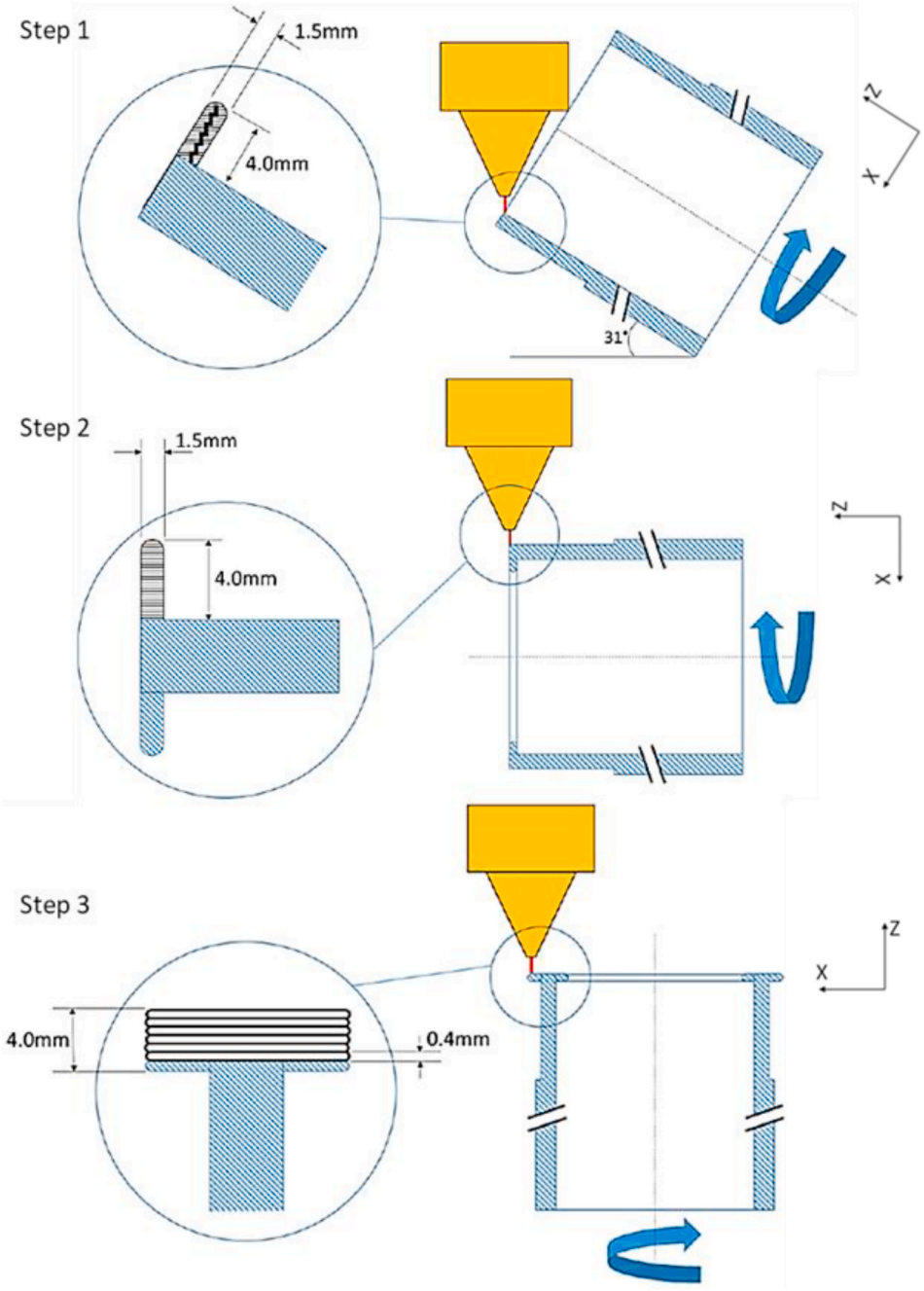

Fig. 2. Steps showing the build methodology and toolpath approach to manufacture the flanges.

edge of the external flange and the pipe rotated whilst the nozzle slowly moved in the -X direction, towards the outer edge of the internal flanges. On completion of each layer, the nozzle was incremented in the +Z direction by a distance equal to the layer height and the nozzle moved back to the outside edge of the external flange. The pipe was repositioned by rotating 180° under the nozzle to reset the start point and the process was repeated until the build height reached approximately 4 mm. The application of a rotating start position at 180° for each consecutive layer was to minimize any possible lack of fusion or excess material build-up that could happen at the start of the track, and which might lead to failures during deposition.

Process parameters were developed using the above approach. During the trials, manufactured flanges were sectioned and then polished at multiple locations, to evaluate the deposit density using white light microscopy. Following the final selection of the optimal parameter set, a final test flange was manufactured and sectioned to investigate the hardness variation across the interface between the pipe and the deposited material. On completion of the process development, six pipes were modified with the flange feature using finalized process parameters which are summarized in Table 2.

Due to limited clearance, the deposition of the internal flange had to have the laser beam incident on the substrate at a shallow angle and apply a slightly higher powder mass rate. This was because an angled beam would deliver a laser spot and powder focused area slightly elongated and enlarged. Therefore, a higher mass flow rate was required to maintain the melt consistency across the enlarged exposure area. However, this arrangement also increased the width of the melt track and thus the thickness of the internal flange wall increases from 1.5 mm to 1.65 mm.

Table 2
Optimal DED process parameters for the manufacturing of the flange.

Process parameters	Internal flange	External flange	Top coating
Laser power (W)	1100		
Scan speed (mm/min)	600		
Laser spot size (mm)	1.5		
Nozzle shielding gas flow rate (litres/min)	5.0		
Powder carrier gas flow rate (litres/min)	2.5		
Nozzle stand-off (mm)	11		
Powder mass flow rate (g/min)	2.4	2.0	2.0
Incremental Z height (mm)	0.2	0.2	0.4
Track separation (mm)	–	–	0.9

3.4. Hardness test

Using the finalized parameters in Table 2, a flange was deposited onto one additional pipe for follow-on investigations of post-clad micro hardness variation across the interface between the pipe and the deposited material. The part was sectioned across the interface followed by micro hardness measurement (Fig. 3). Different zones in the figure are distinguished based on the transverse macro cross-section, the hardness variation that is potentially caused by the deposited powder material, and the areas affected by the heat from the laser DED process. The range of Vickers hardness values fell between 152HV0.1 in the bulk of the substrate to an average value of 225HV0.1 in the bulk of the deposited area. The increase in the hardness in DED deposited material often occurs due to the high cooling rate of the process. There was also a notable excess of material that had built up on the underside of the internal pipe flange (Fig. 4), which was caused by the unused powder falling onto the substrate and was being fused by the laser as it slipped and passed the top of the wall.

3.5. X-ray Computed Tomography

X-ray Computed Tomography (XCT) was conducted to inspect the additively manufactured flange features that were fully non-destructive. For each pipe, a datum wire was attached onto the pipe's outer surface, centrally positioned between the component ID number, to act as a reference in the XCT scan (Fig. 5). For each acquired XCT scan analysis, the wire seen in the captured 3D volume data was referred to the 12 o'clock position.

XCT results showed that DED-manufactured pipe flanges achieved overall good quality with high density and small isolated pores, especially for flanges on pipe No.1, 3, 4, and 5 had only 4–6 pores of any significant size being observed within the entire deposit. The size of the largest pore in each of the pipe flanges 1, 3, 4, and 5 was 0.22 mm, 0.29 mm, 0,26 mm, and 0.22 mm, respectively. Pipe No.6 also exhibited a low level of porosity, which only four pores were detected. The largest pore was approximately 0.33 mm, and there was evidence of lack of fusion at the lower corner of the outer flange, at the interface region between the flange and the substrate. A similar lack of fusion defect was also observed in one region on the underside of deposited flange on the inner surface of the pipe wall.

For pipe No.2, a large number of pores were observed around the circumference of the flange, and they were all situated at the same depth and radial position. And the largest pore was 0.451 mm. This was because the process was interrupted due to the clogged powder nozzle, which reduced the powder deposition rate, thus the quality of the powder focus. This could explain why those pores were seen all located at the same radial and vertical position in the flange. Process was immediately paused by the operator to correct the nozzle power-gas stream, before continuing the deposition.

Although porosities have been identified in each pipe, most of them were very small in diameter and isolated. As there was a subsequent TIG welding process to be conducted, the deposited flange was to be fully re-melted and fused with the base metal. With the application of appropriate welding parameters, pores were highly likely to be eradicated during solidification. Therefore, all AM modified pipes were subjected to machining preparation followed by a TIG welding process.

4. Orbital TIG welding and weld quality assessment

4.1. Process development

Six reference pipes were manufactured (denoted as 'IR' – insert ring) using a semi-automated autogenous orbital TIG welding system to establish a preliminary welding process procedure, according to BS EN ISO 15614–1:2017 + A1:2019. Although the welding process was pre-programmed and fully monitored, and the joint was precisely produced by the orbital welding head, significant manual supervision and adjustments were required during the setup stage. In order to avoid the complexity of gravity-induced inconsistent weld profile, pipe stubs were

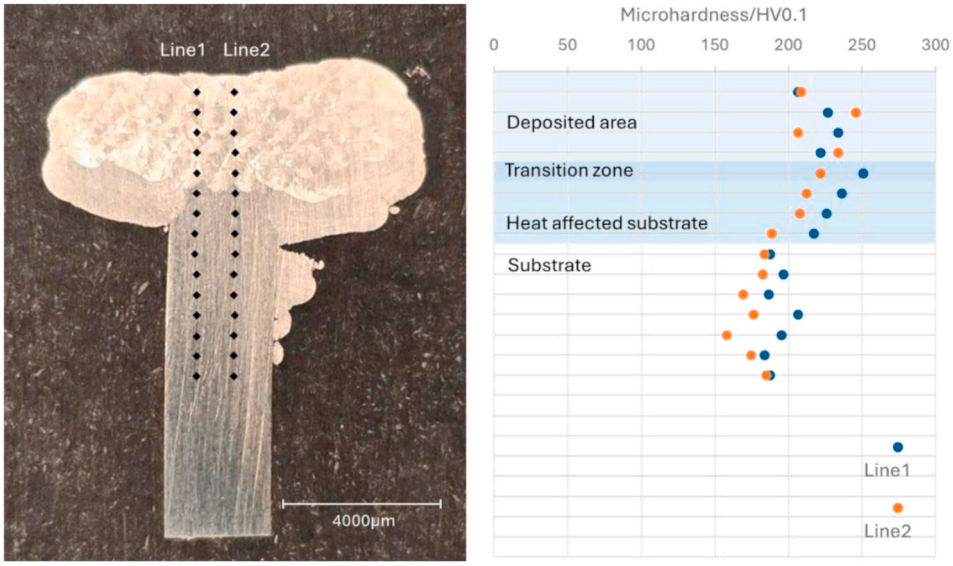

Fig. 3. Indicative locations of the microhardness indentation across the substrate, flange interface, as well as the deposited area.

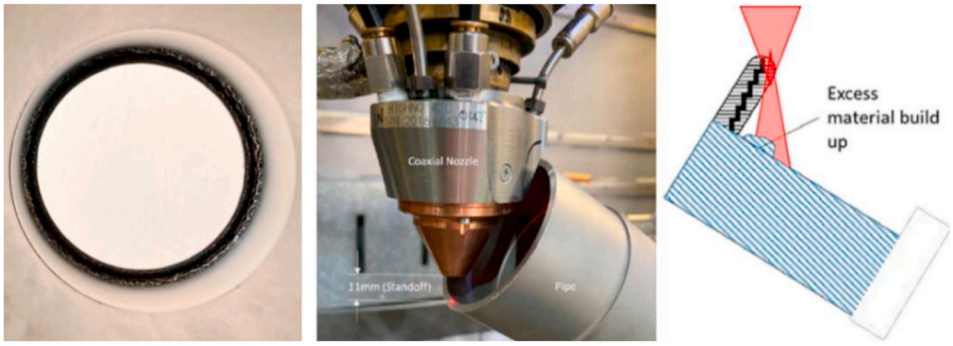

Fig. 4. Excess material builds up at the base of the internal flange due to unused powder being fused by the passing laser as it clips the top of the angled wall.

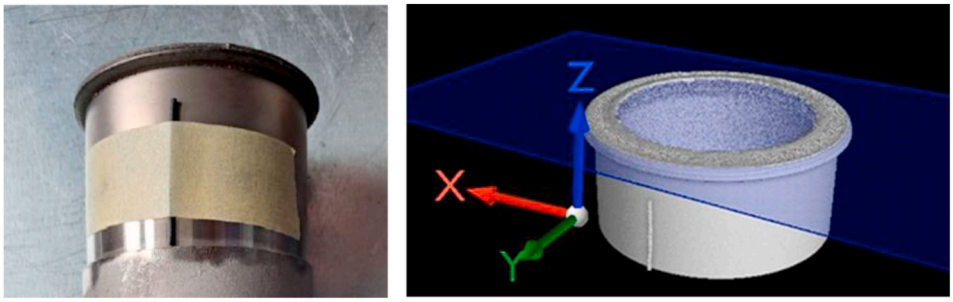

Fig. 5. The wire datum and an example of the acquired 3D XCT image.

set up vertically on the fixture in a 2G welding position. Prior to the welding, an inserted filler ring was firstly placed concentrically between the pipe stubs and then spot welded onto the end of the upper pipe. The filler ring had a dimension of 71.3 mm outer diameter, 63.5 mm inner diameter and 0.7 mm thickness (Fig. 6). It was extracted from the unmachined pipe material, therefore, has an identical chemical composition as the parent metal.

For the six additively modified pipes (denoted as 'LD' – laser deposited), the flanges were firstly machined and then manually filed to the same size as the filler ring as the machining failed to achieve required tolerances. During welding, the pipe stub with the flange feature was positioned on the top with the flange facing downward, which was then TIG welded to the pipe stub underneath. The orbital welding tool was loaded on the lower half pipe, with the welding torch facing the joint area horizontally, and tightly mounted on the welding fixture (Fig. 7). The tungsten tip was 2.4 mm in diameter, with a stick out length of 5 mm, and stood off the material surface 1.6 mm (arc length). Argon shielding gas was delivered coaxially through a 10 mm-diamater nozzle.

This process adopted a method of rotating the torch anticlockwise first with the cables winding up around the pipe before initiating the electric arc. The cables unwound clockwise as the welding took place. Cable management was critical, and it was handled manually. Details of the process parameters are listed in Table 3.

4.2. Non-destructive evaluation

Non-destructive evaluation (NDE) was performed to inspect the welds on their surfaces and in the material volume. Dye penetrant inspection (DPI) was carried out on each weld cap and adjacent parent materials within 20 mm on each side to detect surface breaking flaws. All produced butt welds have passed the DPI examination. It was observed that each finished weld profile was blended smoothly with the parent materials, and no penetrant bleed-out present at the time of the

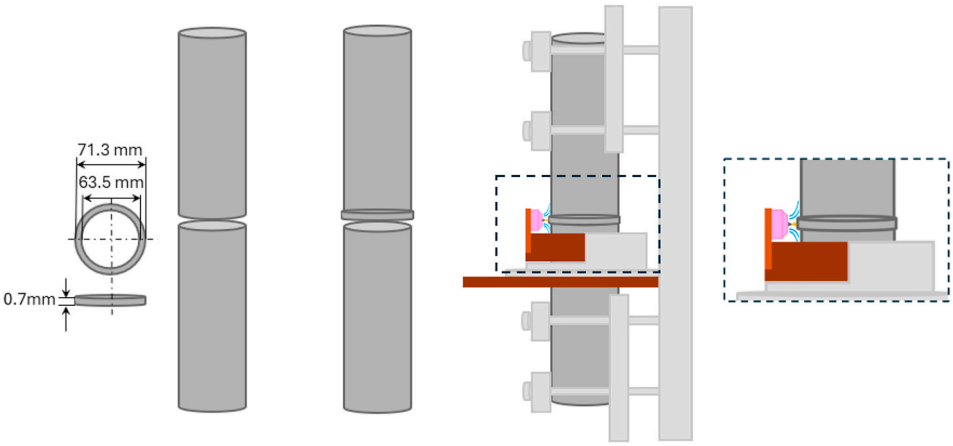

Fig. 6. A schematic of pipe setups and welding configuration for both IR and LD pipes.

Fig. 7. Welding setups showing a 2G orbital autogenous TIG process of additively modified pipe feature.

Table 3
Developed orbital TIG pre-welding process parameters.

Acquired Parameters	Average value (Insert ring)	Average value (AM feature)
Input energy, kJ/mm	0.24–0.25	0.26–0.28
Welding current, A	67.32–67.84	67.28–67.33
Power source welding voltage, V	11–11.7	12.24–12.84
Welding speed, mm/min	109.02–109.89	108.99–109.14
Gas flow, L/min	5	5

test.

X-ray Radiographic inspection was thereafter conducted to assess the weld quality volumetrically, in accordance with BS EN 17636–1: 2022. Due to the small pipe inner diameter, which provided limited access to the bore, four exposures were taken per weld at every 90° using a double-wall double-image (DWDI) technique to achieve 100 % coverage and density. X-ray results showed that the six welds produced with the 'inserted filler ring' were defect free. In comparison, AM modified pipe joint LD3 has been observed with slight misalignment but still qualified as acceptable. Weld LD6 was rejected due to the lack of root fusion. Therefore, LD6 was not pursued with further testing and examinations.

Table 4
Destructive testing carried out on each weld.

Group	Pipe	Tensile test coupon				Bending test coupon				Macro sample		Metallographic examination	
		Weld		UTS (MPa)	Strain	Face		Root					
		main	SS[a]			Weld		Weld		Weld		Microhardness mapping/ Sem-EDX/EBSD	Tensile fracture morphology/SEM-EDX/
						main	SS	main	SS	main	SS		
1	**IR1**		IR1SS	599	0.74	IR1				IR1			
	IR2		IR2SS	563	0.57			IR2		IR2		IR2	IR2SS
	IR3	IR3		584	0.59		IR3SS	IR3					
	IR5					IR5			IR5SS				
	IR6							IR6			IR6SS		
	IR7					IR7					IR7SS		
2[b]	**LD1**	LD1		561	0.76	LD1 (1)	LD1 (1)			LD1-A		LD1-A	LD1
			LD1SS	587	0.89	LD1 (2)	LD1 (2)			LD1-B			
3	**LD2**		LD2SS	577	0.65	LD2		LD2		LD2			
	LD3	LD3		597	0.65	LD3			LD3SS	LD3		LD3	LD3
	LD4	LD4		577	0.57	LD4			LD4SS				
	LD5					LD5			LD5		LD5SS		
	LD6	Failed in X-ray Radiographic Inspection											

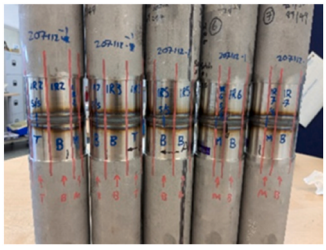

Group1

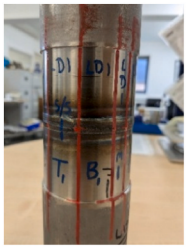

Group 2

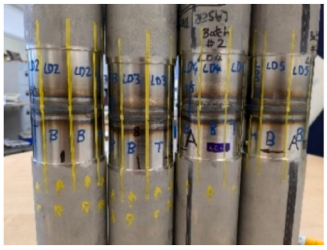

Group 3

[a] Weld start/stop denoted as 'SS'.
[b] Group 2 were solely extracted from LD1 as it has been re-welded multiple times, which possessed a distinctive thermal history and joint profile.

4.3. Destructive testing

Welds that have passed the X-ray inspection were grouped into three sets and subjected to tensile testing (BS EN ISO 4136: 2022) and bend (BS EN ISO 5173: 2023 – three point bend) tests to compare the mechanical properties of the welds. Pipes in group 1 were fabricated with the filler rings. Test specimens in Group 2 were solely extracted from LD1 as it has been re-welded multiple times, which possessed a distinctive thermal history and joint profile. Pipes in group 3 had AM modified features. In each pipe, the test specimens were extracted randomly at multiple locations along the weld, including the welding start/stop (SS) area (Table 4). Bending was performed on the specimens with both face bend and root bend tests. In addition, macroscopic examination was performed (BS EN ISO 17639: 2022) on the cross-sections of the selected welds.

The primary objective of the tensile testing was to provide a comparison of the tensile strengths of the welds that were from different material compositions, which the AM feature was manufactured from commercially available 316L powder, while the filler ring had an identical composition to the parent material. Engineering stress and strain of the tested specimens are listed in Table 4. It is worth noting that tensile strength here was not used to qualify a welding procedure, although it has met the level 1 requirement according to BS EN ISO 15614. Most of the specimens fractured at their welds, except for LD1SS which failed at its parent metal. The ultimate tensile strengths of all the tested specimens were within the range of 515–690 MPa, which was required in the material specification of sourced stainless steel 316L, although the parent pipe material was reported at the value of 597 MPa.

The engineering stress-strain curves (Fig. 8) suggested that all the welds have shown to have good ductility. Most of the specimens fractured at their welds, which LD4 had the lowest strain of approximate 0.57. In comparison, LD1SS which failed at its parent metal showed a much higher strain of over 0.89 at fracture. Compared to the LD pipe joints, overall IR pipe welds were less ductile, although IR1SS fractured at higher strain than that of IR2SS and IR3. There was an obvious interruption at the early stage of the tension observed from the stress-stain curve of IR1SS, which the test specimen was not tightly gripped at the beginning. Therefore, the initial-stress-strain curve showed an artifact caused by the take-up of slack or seating of the specimen in the grips, leading to an artificially low initial stiffness.

All the bending test specimens have passed testing and are deemed acceptable (BS EN ISO 5173: 2023 – three point bend). For the samples performed with macroscopic examination, Group 1 and 2 showed no significant welding-related defects apparent within the sections examined. However, plate misalignment was observed in LD2 and LD5, which still met the acceptance criteria (BS EN ISO 5173: 2023 – three point bend). For LD1, sample LD1-B had 0.13 mm root concavity, which was not acceptable, according to BS EN ISO 5817 (quality level B). Tensile and macro samples from each group were selected for further metallographic examination. Taking out the most ductile sample LD1SS which failed at its parent material, and the least ductile sample LD4 from the test results, apart from LD1, samples from IR and LR failed at similar strain, respectively. Therefore, one representative sample was selected from each group to perform a metallographic examination.

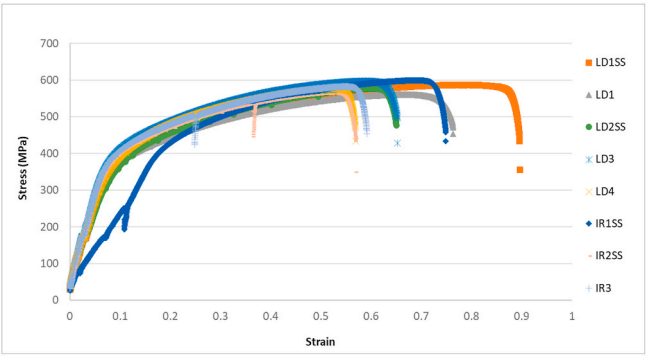

Fig. 8. Engineering tensile stress-strain curves of selected welds.

4.4. Metallographic examination

4.4.1. Microhardness mapping

Samples LD1-A, IR2 and LD3 were further prepared for metallographic examination. On each sample, hardness mapping was performed across its weld, HAZ and adjacent parent material using Vickers indentation, covering an area of 2.5 mm × 3.5 mm, and included a total of 300 indents (Fig. 9). This was kept consistent for all three samples to ensure uniform data collection, enabling comparisons between the different regions.

The average line hardness was calculated by taking measurements at 15 points across the HAZ, weld, and parent material respectively. The average values of the hardness were quite similar, indicating there was no significant hardening or softening of the joint and the adjacent material after the welding, albeit small variations were observed in the hardness mappings (Fig. 10). Among three samples, LD1-A exhibited the most uniform hardness magnitude across the entire joint area. In contrast, IR2 and LD3 have revealed localized hardness reduction in the areas around the fusion line and near the weld centre.

4.4.2. Fracture morphology

Reduction in width of the cross-section over 80 % and significant necking were observed in the tensile specimens LD1, IR2SS and LD3 under optical microscopy. High resolution images were generated using Scanning Electron Microscopy (SEM). A dimpled feature on the fracture surfaces of the specimens along with the presence of tearing ridges or shear lips around the edges has been observed (Fig. 11), suggesting that the fracture mode was ductile.

4.4.3. Compositional analysis

The elemental and compositional analysis, on the cross-section of the weld, HAZ, and parent metal, as well as the fracture surface for each sample, was performed using SEM combined with Energy-Dispersive X-ray Spectroscopy (SEM-EDX/EDS). Bulk chemical composition, quantified from the EDS maps, has shown that three samples had very similar compositional contents, and there were no significant variations in chemical composition across all the regions.

Micro-segregation of Chromium (Cr)and Nickel (Ni) was identified in the weld and the narrow region next to the fusion line in all the samples, in which the area with a high concentration of Cr exhibited a low concentration of Ni. In addition, EDS maps have revealed the presence of inclusions primarily composed of oxygen (O), Aluminium (Al), manganese (Mn), and S, with a reduced iron content in the welds as well as at the fractured surfaces, and in the HAZs, suggesting these inclusions were likely oxides and sulphides which were trapped in the material during the welding processes (Fig. 12).

In the welds and HAZ regions, the inclusions were predominantly in a spherical shape, which in comparison, in the parent metals, some particles appeared in an elongated shape (Fig. 13). This was further studied by analysing the inclusion in LD1-A parent material through elemental mapping together with EDS spectra. The results have suggested that the inclusions were primarily Al_2O_3 alongside the MnS, which were the most prevalent types of inclusion in 316L stainless steel.

4.4.4. Grain analysis

Electron Backscattered Diffraction (EBSD) was performed with SEM on cross-section of the samples to further analyse the grain morphology and crystallographic properties. For each sample, approximately 2000 grains were analysed. From the inverse pole figures (IPF) of the fusion zones in Fig. 14, LD3 has shown a distinctive grain structure, which the fusion boundaries were more obvious to identify. The coarse columnar

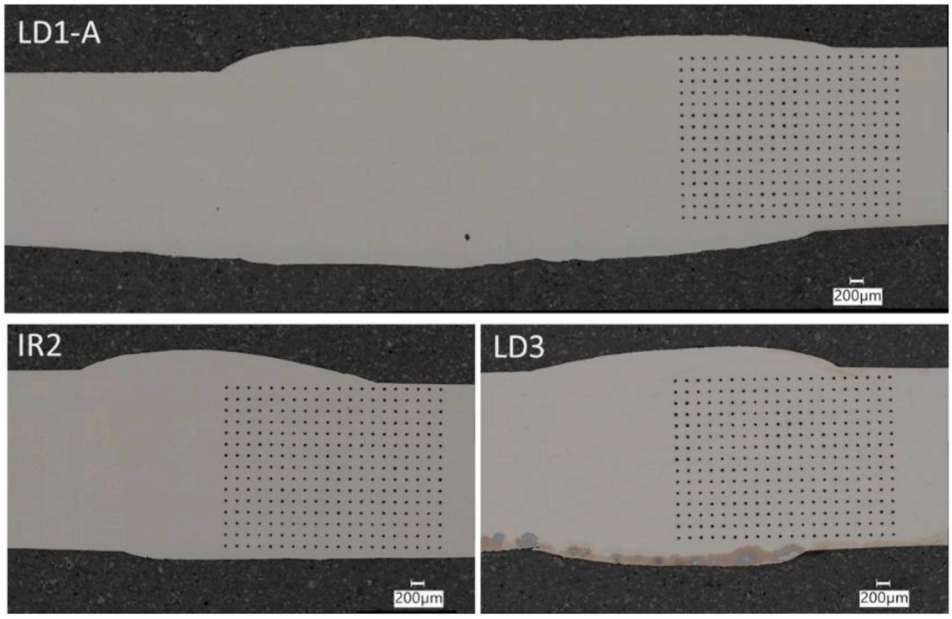

Fig. 9. Observation of the transverse weld cross sections with microhardness indentation under optical microscopy.

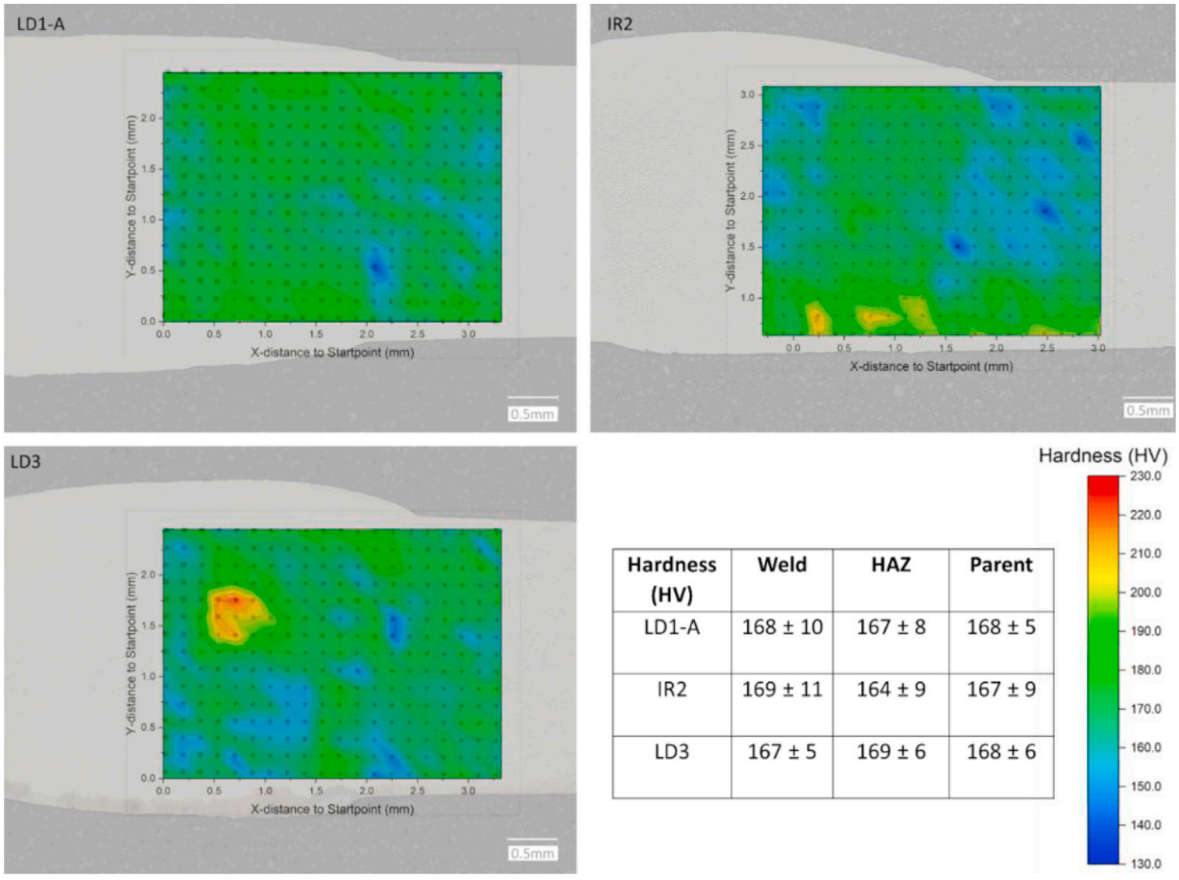

Hardness (HV)	Weld	HAZ	Parent
LD1-A	168 ± 10	167 ± 8	168 ± 5
IR2	169 ± 11	164 ± 9	167 ± 9
LD3	167 ± 5	169 ± 6	168 ± 6

Fig. 10. Hardness mapping of the samples showing small variations across the weld, HAZ and parent metal.

grains were observed growing from the HAZ perpendicular to the fusion line, in the direction of the largest thermal gradient, toward the weld centre. Near the weld centreline where the columnar grains intersect, finer equiaxed grains were formed. However, LD1-A has shown a similar grain structure to that of IR2, which the fusion boundaries were not distinctive from the parent materials, but with larger and more elongated grains in the fusion zone.

LD1-A was counted with the highest fraction (23.6 %) of low-angle grain boundaries (LAGBs, 2–10°, grey lines in Fig. 14), which indicates the lowest fraction of recrystallization. This means, although the weld area has undergone significant thermal deformation, it was not enough to lead to significant recrystallization. LAGBs are the interfaces

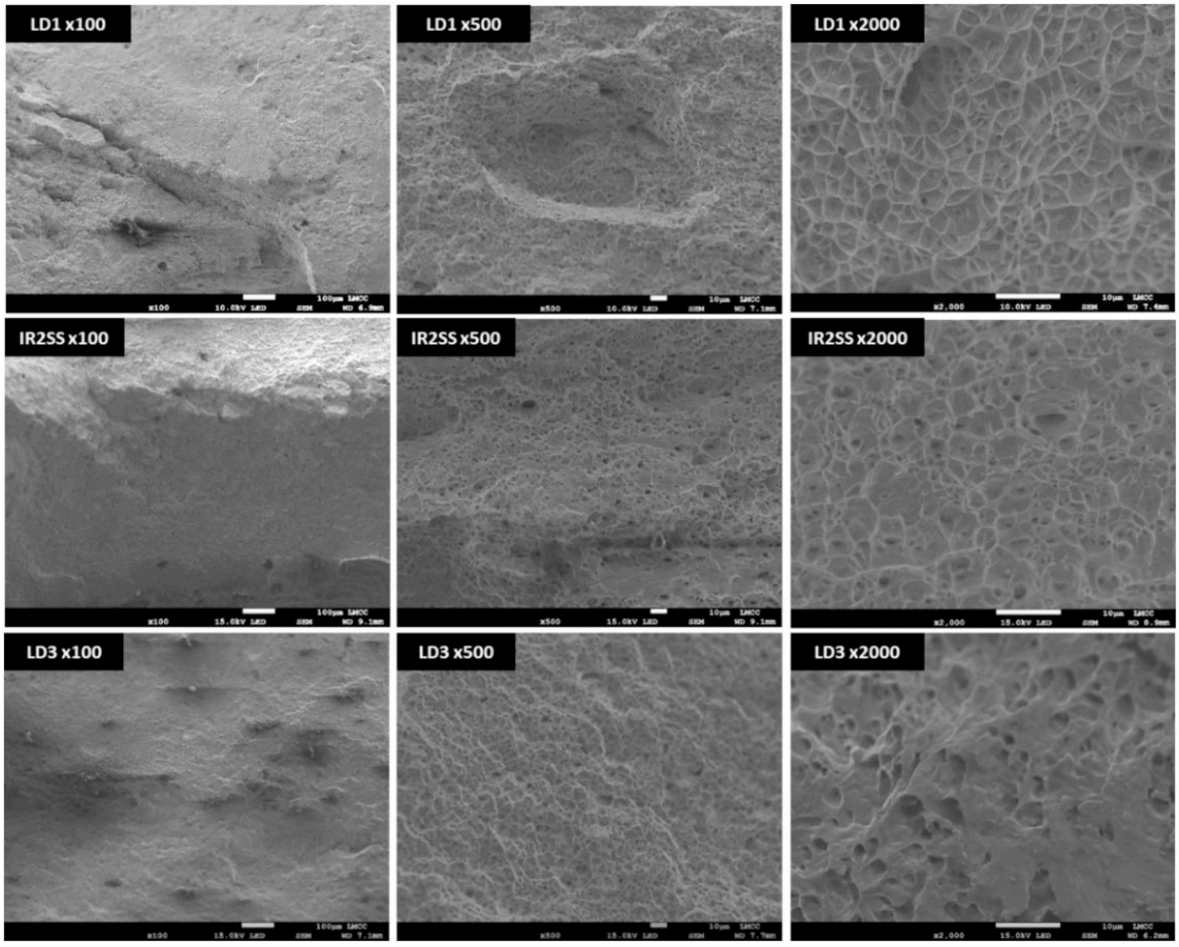

Fig. 11. Fracture tomography of the tensile samples under SEM.

between grains with small misorientations and are sociated with deformation and evolving substructure inside individual grains. During recrystallization, LAGBs are often converted into high-angle grain boundaries (HAGBs, >10°, black lines in Fig. 14) as the new grains grow and consume the deformed microstructures. Therefore, a high fraction of LAGBs suggests that the recrystallization process is incomplete or has not occurred to a significant extent.

Recrystallization fraction maps were generated for the welds using Grain Orientation Spread (GOS) to identify recrystallized grains (Fig. 15). This method focuses on grain-wide variations, enabling quantitative analysis of recrystallization. Grains with GOS value below the common threshold value of 2° are considered recrystalized or non-deformed, offering insights into the extent of recrystallization in different regions of the weld. Among three weld samples, a high fraction of low GOS value suggests that LD3 has a microstructure with the highest proportion (95 %) of recrystallized or relaxed grains. In other words, the grains in LD3 have a low degree of deformation.

In addition, GOS maps also provide a qualitative understanding of the residual stress in a weld, by indicating the areas with different stress levels through the patterns of grain orientation. Therefore, a higher fraction of high GOS in LD1-A suggests that significant residual stresses, compared to IR2 and LD3, were introduced to the joint during the processes. GOS maps were not processed for parent materials because they have undergone minimal microstructural changes compared to the weld and HAZ. The parent material was largely unaffected by the welding process, therefore, experiencing negligible deformation or recrystallization.

5. Discussion

5.1. AM and welding on material mechanical properties

The welding process developed in this study allowed for the successful fabrication of nuclear graded 316L stainless steel pipes, either by applying an inserted filler ring or by welding on to an AM produced feature. Although pores and lack of fusion have been identified in the AM produced parts, they were successfully eradicated during the subsequent welding process.

Welded metals have shown significant elongation at fracture and a dimpled fracture face morphology indicated that the joints had very good ductility. This was also reflected in the overall hardness, which there was no significant variation across the weld region and parent material. Although the hardness in the laser DED-manufactured flange was measured with higher values than that in the base metal (Fig. 3), the overall hardness magnitude decreased in the fusion zone after TIG welding (Fig. 9). Similar results were found in previous studies that laser DED manufactured 316L parts had higher hardness compared to those manufactured using conventional methods [39–42]. Due to the rapid heating and cooling, laser DED often leads to refined grain sizes and high dislocation densities within the microstructure, thus introducing higher hardness compared to conventionally produced 316L parts. Other research also presented that 316L welds produced from additively manufactured parts have shown reduction in hardness in the fusion zone [43–45]. This is because the welding process provides high energy input, which results in a slower cooling rate, therefore provided more time for grain growth during solidification, and potentially led to reduced indentation hardness [43].

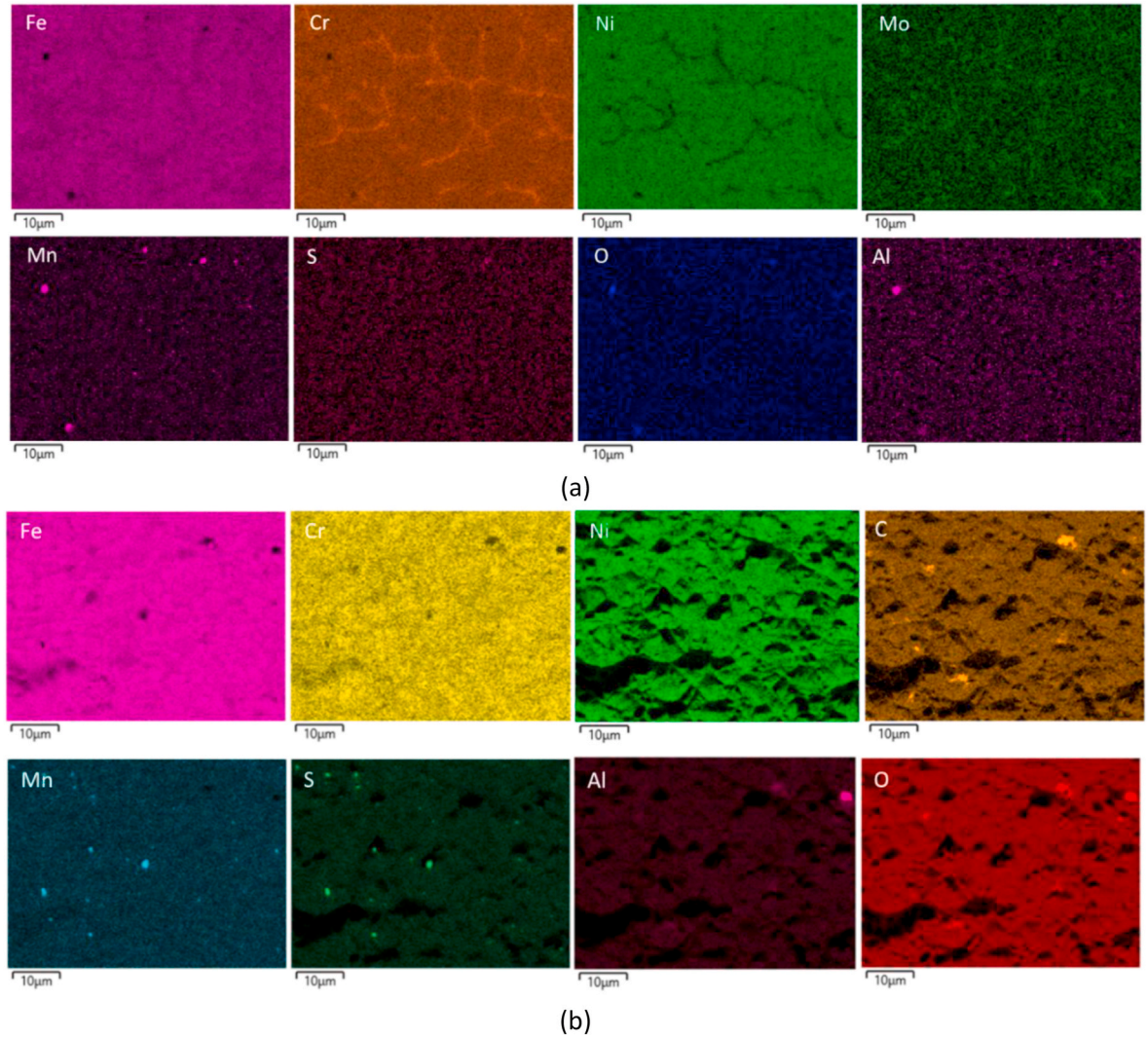

Fig. 12. SEM-DEX maps showing the micro-segregation and inclusions (a) in LD3 fusion zone (b) at IR2SS weld fracture surface.

5.2. AM and welding on material microstructures

Although manufactured from the identical process procedures, LD1-A did not show a similar grain structure as that within LD3. This was because during the fabrication of LD1, the pipe stub with the AM manufactured flange was positioned underneath with the feature facing up. Due to the gravity impact, the flange feature could not be fully fused into the top pipe stub after welding. Therefore, the joint area was repaired using the same welding parameters with a shift of the tungsten tip position 500 μm upwards axially. Repair welding was performed four times until a proper joint was achieved. A final compliant joint was produced after the tungsten tip shifted 2 mm where the microstructure of the weld mostly evolved from melting the parent material. In other words, the microstructure evolution in the cross-sectioned area of LD1-A is similar to that of IR2.

During welding, often if the welding process does not provide enough heat or the material does not remain at the high enough temperature for a sufficient duration, recrystallization may be incomplete. Incomplete recrystallization also led to higher residual stresses [46]. Although all the welds in this study were produced using strictly controlled process procedures, IR2 and LD3 exhibited different extent of recrystallization, which could be a result of the form of material properties such as the chemical composition and the initial microstructures [47]. In contrast, the exacerbation of incomplete recrystallization in LD1 could result from the repeated re-welding, in which the processes introduced new stresses and microstructural changes. This is because the microstructure and defect density are different in deformed matrix and partially recrystallized grains, which leads to stress concentration and strain gradients [48,49]. And it is worth noting that only LD1 was fractured at its parent material, which also confirmed that LD1 had a different stress state.

5.3. AM and welding on material composition

In an autogenous welding process, micro-segregation is often pronounced in the weld as is no external filler added to buffer the non-uniform alloying element redistribution during solidification. Therefore, the joint is solely derived from the base metal. Particularly for welding of 316L, which often first forms primary δ-ferrite and then partially transforms to austenite as it solidifies. Cr micro-segregation occurs during dendrite growth due to the lower solubility of Cr in solid (δ-ferrite) than that in liquid, resulting in Cr being rejected into the liquid phase, forming Cr-depleted dendrite cores and Cr-enriched interdendritic regions [50]. Welding is a non-equilibrium process which involves rapid solidification coupled with a significant thermal gradient. There is also limited time for diffusion of the solute.

One of the strategies to reduce micro-segregation is to introduce over-alloyed filler wire, which allows for the dilution or balance of the

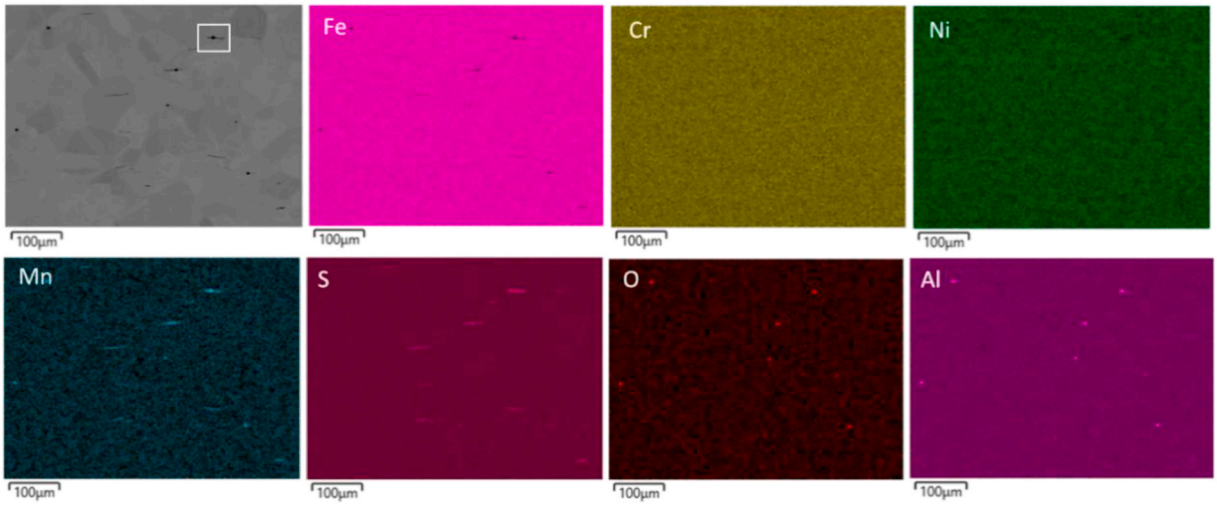

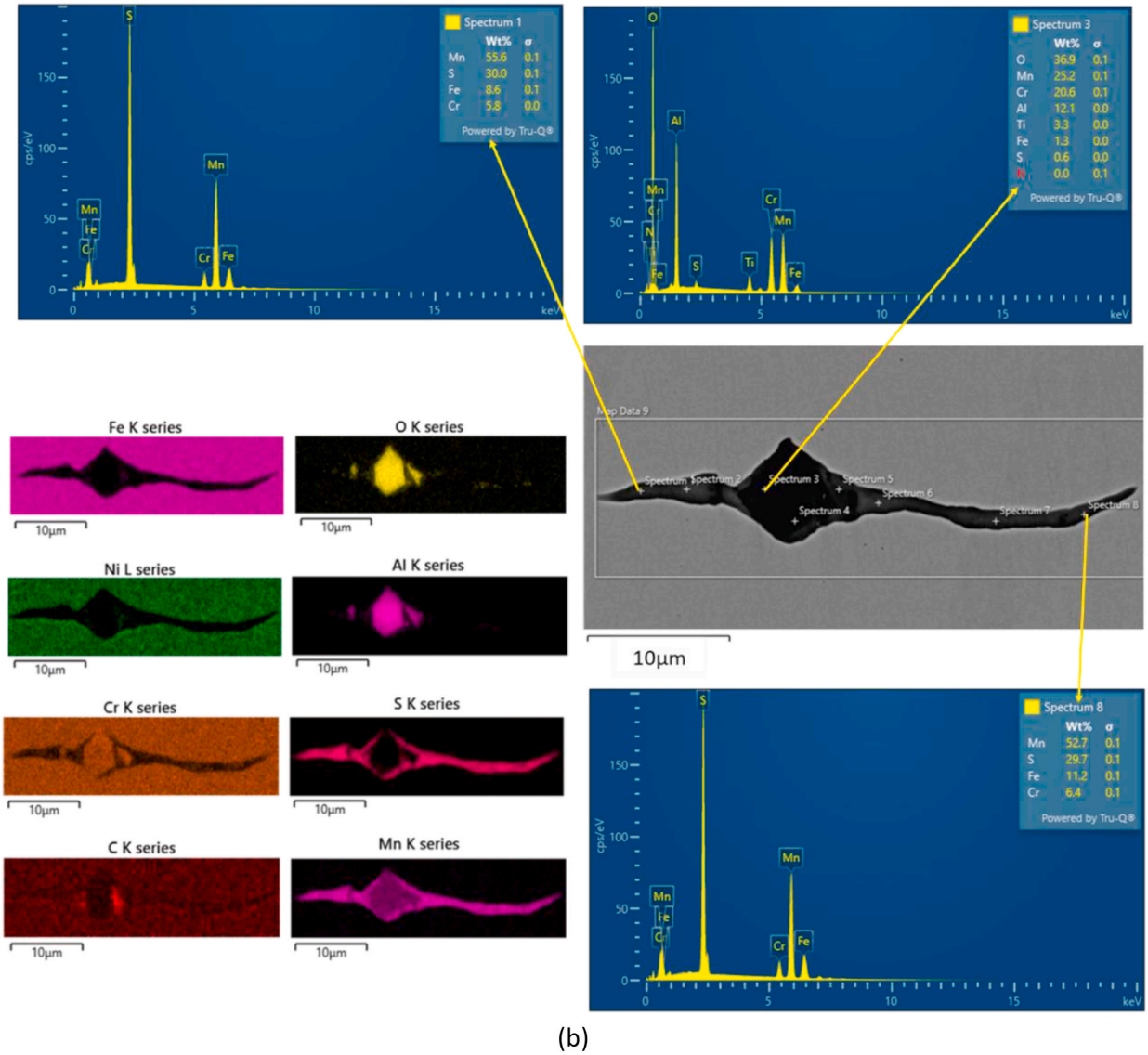

Fig. 13. Inclusion analysis in LD1-A parent material using elemental mapping together with EDS spectra.

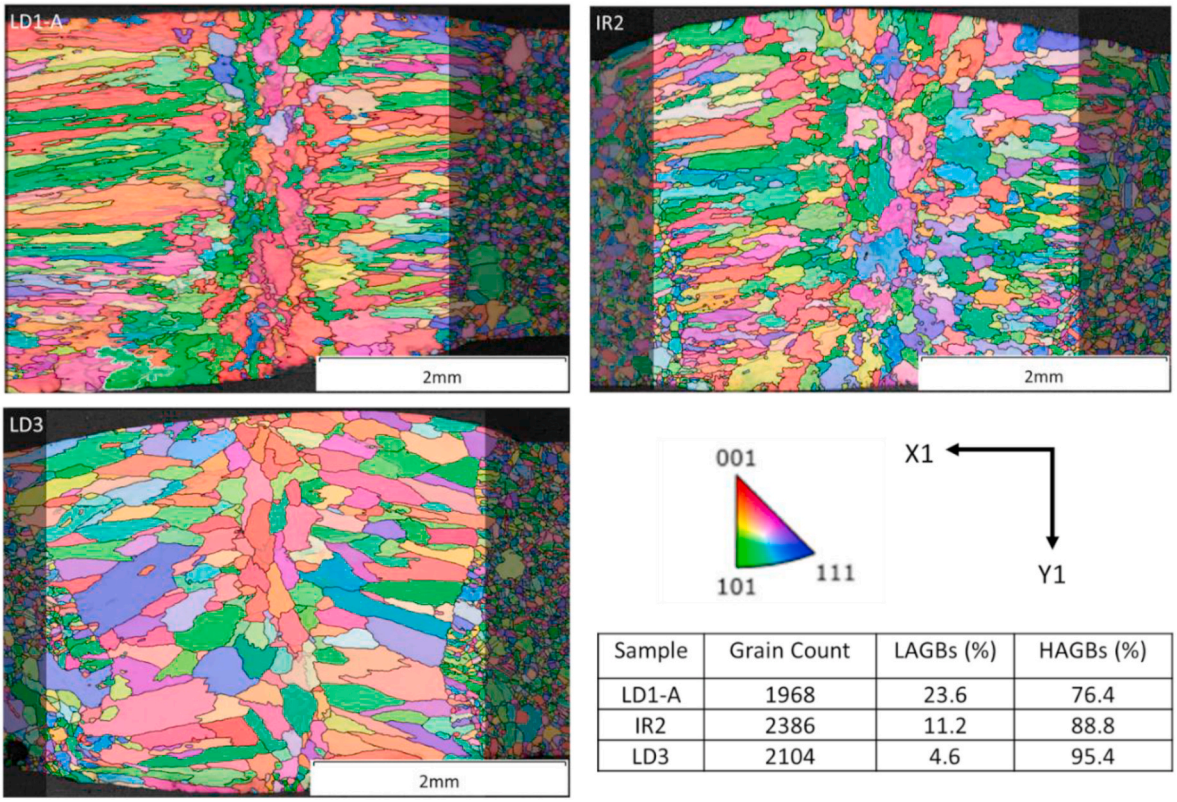

Sample	Grain Count	LAGBs (%)	HAGBs (%)
LD1-A	1968	23.6	76.4
IR2	2386	11.2	88.8
LD3	2104	4.6	95.4

Fig. 14. Inverse pole figures (IPF) of the fusion zones.

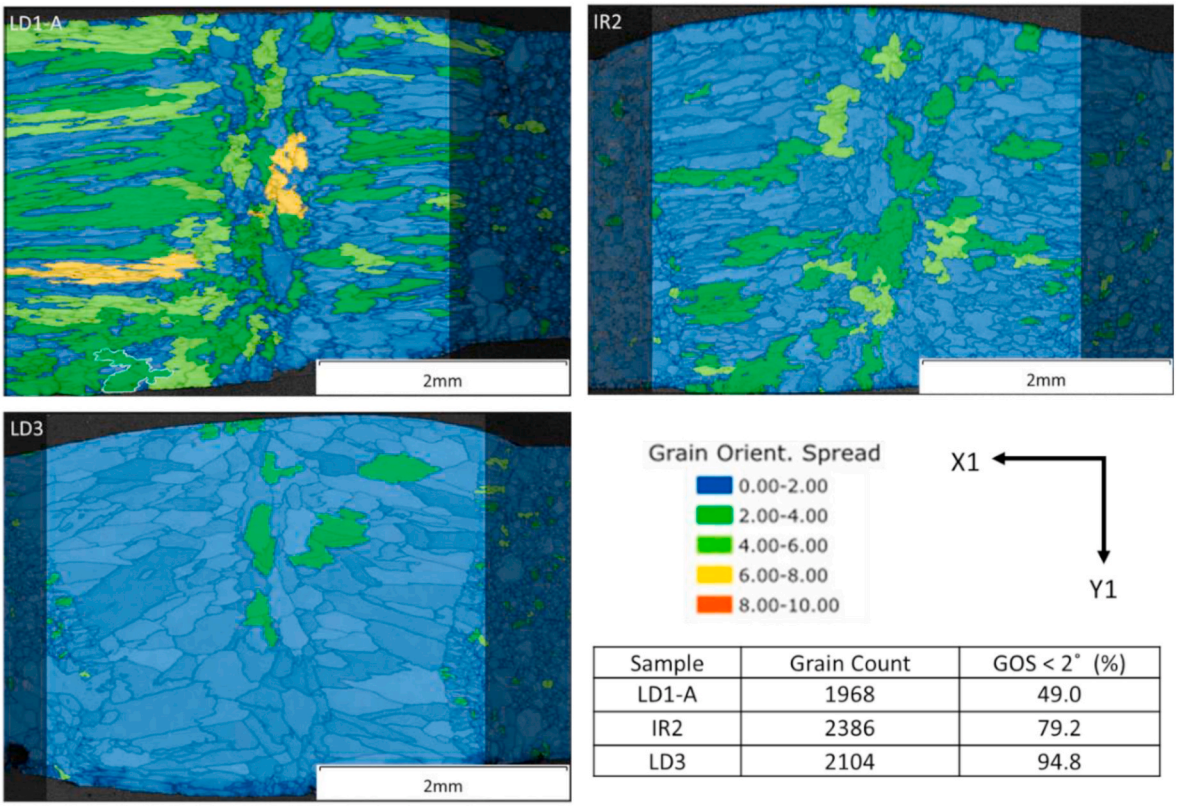

Sample	Grain Count	GOS < 2° (%)
LD1-A	1968	49.0
IR2	2386	79.2
LD3	2104	94.8

Fig. 15. Recrystallization fraction maps of the fusion zones.

segregating elements. However, as mentioned early on this would not be viable for remote handling. In this study, micro-segregation was identified in examined 316L autogenous welds. Albeit the powder material used for depositing the AM feature had slightly higher content in Cr and Ni, compared to the pipe base metal, such low-level elemental enrichment in the composition has not effectively mitigated the micro-segregation.

Both fusion-based processes involve localized high heat input which can cause loss of volatile alloying elements, such as Cr evaporation, from the molten pool and surrounding areas [51–54]. The metal chemistry was not evaluated throughout the entire development; thus, it is unknown the extent of element loss after laser DED and TIG welding processes, respectively. Future work may involve tailoring the composition of the powder feedstock for additive manufacturing by taking into account alloying element loss from the processes. Optimisation of the Cr/Ni ratio as well as welding parameters is another critical area to be investigated [55,56].

5.4. AM and welding on joint design

In this feasibility study, welding was carried out with the pipe stubs positioned vertically. This was to reduce the complexity of the gravitational influence on achieving the required weld profile. In the case of welding horizontal pipes, a slightly higher metal volume in a pipe stub, which is either additively manufactured or machined from a heavy duty walled pipe, can cause non-uniformly distributed heat and arc instability, leading to potential uneven penetration, distortion and lack of fusion at the joint. In contrast, spot welding of the filler ring onto the pipe stub solely creates a mechanical joint. The method was adopted as it successfully eliminated the aforementioned issues [36], albeit remote handling solutions are still unavailable to precisely align the pipe stubs, control the positioning and the attachment of the filler ring, and subsequent material fusion in the 5G welding position.

One possible approach for tube joining is to utilize a cuffed end design, which may be welded autogenously. However, this approach is not suitable for larger pipes. For fusion cooling pipes, subtracting such features from heavy-duty walled pipes is not economically viable. The ‘cuff’ design has the advantage of providing a tight fit, whereas also introducing constrains during alignment. This means machining tolerances must be extremely high to guarantee the fit-up and alignment during remote handling. From this perspective, an additively manufactured filler ring feature has higher flexibility. Besides, to avoid the issues caused by uneven heat distribution, the feature may be manufactured on the end of both pipe stubs, followed by machining to desired dimensions. This, on the other hand, has the potential to reduce the gravity impact while welding in a challenging orientation.

5.5. AM potentials for the use in fusion

Since additive manufacturing is economical for rapid prototyping, other joint designs can be explored so as to enable remote operations, especially where in-situ processes using remotely deployed tools are limited, then the component customization can be prepared ex-situ. Other potentials for using additive manufacturing in fusion include restoring component physical geometry, modifying metallurgical composition, conducting repair and refurbishment, in situ or ex situ. For instance, disconnecting welded cooling pipes involves removing the joint and adjacent heat-affected areas, or an even larger section if required, which shortens the pipe’s length hence limiting the number of times for re-welding. Additive manufacturing allows for rebuilding the pipe wall to restore the length, at the same time introducing bespoke joint design with optimized chemical composition to achieve robust welds. Repair of welds and pipe parts may be required during commissioning and service life. In addition to the need for developing remote handling tools and automated systems for in-situ processes, component recycling and refurbishing may be performed in a hot cell environment designated for ex-situ maintenance, which could also lead to extended component lifespan and reduction of waste.

6. Conclusion

This work investigated the use of laser DED to deposit material as an alternative approach to using filler rings for fabricating nuclear graded 316L cooling pipes. The AM manufactured parts were tested and showed good quality. A semi-automated autogenous TIG welding process was thereafter conducted on the AM modified pipes followed by a series of mechanical and metallurgical testing. The results suggest that the overall concept of using AM has shown promise and was able to produce compliant welded pipe joints, implying potential improvements to the maintenance strategies for future fusion power plants and experimental devices.

CRediT authorship contribution statement

Yao Ren: Writing – original draft, Resources, Project administration, Methodology, Formal analysis, Conceptualization. **Robert Skilton:** Writing – review & editing, Conceptualization. **Ian Merrigan:** Writing – review & editing, Methodology, Data curation. **Neil Mayfield:** Methodology, Data curation.

Declaration of competing interest

The authors declare that they have no known competing financial interests or personal relationships that could have appeared to influence the work reported in this paper.

Acknowledgements

This work has been funded by the EPSRC Energy Programme [grant number EP/W006839/1]. To obtain further information on the data and models underlying this paper please contact PublicationsManager @ukaea.uk.

References

[1] Nuclear fusion power. https://world-nuclear.org/information-library/current-and-future-generation/nuclear-fusion-power, 2022. November 4, 2025.
[2] Y. Ren, R. Skilton, A review of pipe cutting, welding, and NDE technologies for use in fusion devices, Fusion Eng. Des. 202 (2024), https://doi.org/10.1016/j.fusengdes.2024.114396.
[3] S.C. Prager, F. Najmabadi, Fusion Reactor, Britannica, 2024.
[4] UK Fusion Materials Roadmap 2021-2040, 2021.
[5] S. Jones, Advanced manufacturing applied to nuclear fusion—challenges and solutions, JPhys Energy 5 (2023), https://doi.org/10.1088/2515-7655/acf687.
[6] M. Victoria, N. Baluc, P. Spätig, Structural materials for fusion reactors, Nucl. Fusion 41 (2001) 1047–1053, https://doi.org/10.1088/0029-5515/41/8/308.
[7] H. Neuberger, J. Rey, M. Hees, E. Materna-Morris, D. Bolich, J. Aktaa, et al., Selective Laser sintering as manufacturing process for the realization of complex nuclear fusion and high heat flux components, Fusion Sci. Technol. 72 (2017) 667–672, https://doi.org/10.1080/15361055.2017.1350521.
[8] S. Bonk, H. Neuberger, D. Beckers, J. Koch, S. Antusch, M. Rieth, Additive manufacturing technologies for EUROFER97 components, J. Nucl. Mater. 548 (2021), https://doi.org/10.1016/j.jnucmat.2021.152859.
[9] C. Koehly, H. Neuberger, L. Bühler, Fabrication of thin-walled fusion blanket components like flow channel inserts by selective laser melting, Fusion Eng. Des. 143 (2019) 171–179, https://doi.org/10.1016/j.fusengdes.2019.03.184.
[10] Y. Zhong, L.E. Rännar, S. Wikman, A. Koptyug, L. Liu, D. Cui, et al., Additive manufacturing of ITER first wall panel parts by two approaches: selective laser melting and electron beam melting, Fusion Eng. Des. 116 (2017) 24–33, https://doi.org/10.1016/j.fusengdes.2017.01.032.
[11] E. Karayel, Y. Bozkurt, Additive manufacturing method and different welding applications, J. Mater. Res. Technol. 9 (2020) 11424–11438, https://doi.org/10.1016/j.jmrt.2020.08.039.

[12] X. Zhang, F. Liou, Introduction to additive manufacturing, in: J. Pou, A. Riveiro, J. P. Davim (Eds.), Addit Manuf, Elsevier, 2021, pp. 1–31.
[13] L. Forest, J. Aktaa, L.V. Boccaccini, T. Emmerich, B. Eugen-ghidersa, G. Fondant, et al., Status of the EU DEMO breeding blanket manufacturing R&D activities, Fusion Eng. Des. 152 (2020), https://doi.org/10.1016/j.fusengdes.2019.111420.
[14] J. Feng, P. Zhang, Z. Jia, Z. Yu, C. Fang, H. Yan, et al., Microstructures and mechanical properties of reduced activation ferritic/martensitic steel fabricated by laser melting deposition, Fusion Eng. Des. 173 (2021), https://doi.org/10.1016/j.fusengdes.2021.112865.
[15] J. Fu, On the Powder Metallurgy, Additive Manufacturing and Welding of Oxide Dispersion Strengthened Eurofer Steel, Delft University of Technology, Dissertation, 2021, https://doi.org/10.4233/uuid:b9fbf8e5-dc31-4da0-b560-79c05ebc00a2.
[16] R.E. Nygren, R.R. Dehoff, D.L. Youchison, Y. Katoh, Y.M. Wang, C.M. Spadaccini, et al., Advanced manufacturing—A transformative enabling capability for fusion, Fusion Eng. Des. 136 (2018) 1007–1011, https://doi.org/10.1016/j.fusengdes.2018.04.055.
[17] J. Xie, H. Lu, J. Lu, X. Song, S. Wu, J. Lei, Additive manufacturing of tungsten using directed energy deposition for potential nuclear fusion application, Surf. Coat. Technol. 409 (2021), https://doi.org/10.1016/j.surfcoat.2021.126884.
[18] G. Marinelli, F. Martina, S. Ganguly, S. Williams, Development of Wire + Arc additive manufacture for the production of large-scale unalloyed tungsten components, Int. J. Refract. Metals Hard Mater. 82 (2019) 329–335, https://doi.org/10.1016/j.ijrmhm.2019.05.009.
[19] A.V. Müller, G. Schlick, R. Neu, C. Anstätt, T. Klimkait, J. Lee, et al., Additive manufacturing of pure tungsten by means of selective laser beam melting with substrate preheating temperatures up to 1000 ∘C, Nuclear Mater. Energy 19 (2019) 184–188, https://doi.org/10.1016/j.nme.2019.02.034.
[20] D. Wang, C. Yu, X. Zhou, J. Ma, W. Liu, Z. Shen, Dense pure tungsten fabricated by selective laser melting, Appl. Sci. 7 (2017), https://doi.org/10.3390/app7040430.
[21] C. Tan, K. Zhou, W. Ma, B. Attard, P. Zhang, T. Kuang, Selective laser melting of high-performance pure tungsten: parameter design, densification behavior and mechanical properties, Sci. Technol. Adv. Mater. 19 (2018) 370–380, https://doi.org/10.1080/14686996.2018.1455154.
[22] D. Dorow-Gerspach, A. Kirchner, T. Loewenhoff, G. Pintsuk, T. Weißgärber, M. Wirtz, Additive manufacturing of high density pure tungsten by electron beam melting, Nuclear Mater. Energy 28 (2021), https://doi.org/10.1016/j.nme.2021.101046.
[23] H. Zhang, P.R. Carriere, E.D. Amoako, C.D. Rock, S.U. Thielk, C.G. Fletcher, et al., Microstructure and elevated temperature flexure testing of tungsten produced by electron beam additive manufacturing, JOM 75 (2023) 4094–4107, https://doi.org/10.1007/s11837-023-06045-5.
[24] F. Pixner, R. Buzolin, F. Warchomicka, A. Pilz, N. Enzinger, Wire-based electron beam additive manufacturing of tungsten, Int. J. Refract. Metals Hard Mater. 108 (2022), https://doi.org/10.1016/j.ijrmhm.2022.105917.
[25] S. Mohanty, K. Gokuldoss Prashanth, Metallic coatings through additive manufacturing: a review, Materials 16 (2023) 2325, https://doi.org/10.3390/ma16062325.
[26] R.F. Vaz, A. Garfias, V. Albaladejo, J. Sanchez, I.G. Cano, A review of advances in cold spray additive manufacturing, Coatings 13 (2023), https://doi.org/10.3390/coatings13020267.
[27] S. Yin, P. Cavaliere, B. Aldwell, R. Jenkins, H. Liao, W. Li, et al., Cold spray additive manufacturing and repair: fundamentals and applications, Addit. Manuf. 21 (2018) 628–650, https://doi.org/10.1016/j.addma.2018.04.017.
[28] R. Neu, H. Maier, B. Böswirth, S. Elgeti, H. Greuner, K. Hunger, et al., Investigations on cold spray tungsten/tantalum coatings for plasma facing applications, Nuclear Mater. Energy 34 (2023), https://doi.org/10.1016/j.nme.2022.101343.
[29] J. Cizek, M. Vilemova, F. Lukac, M. Koller, J. Kondas, R. Singh, Cold sprayed tungsten armor for tokamak first wall, Coatings 9 (2019), https://doi.org/10.3390/coatings9120836.
[30] J. Cheng, Y. Xing, E. Dong, L. Zhao, H. Liu, T. Chang, et al., An overview of laser metal deposition for cladding: defect formation mechanisms, defect suppression methods and performance improvements of laser-cladded layers, Materials 15 (2022), https://doi.org/10.3390/ma15165522.
[31] P. Aubry, F. Lomello, O. Hercher, W. Pacquentin, C. Blanc, P.-F. Giroux, et al., Additive manufacturing for nuclear applications, Sustain. Nuclear Energy Technical Platform (2021). www.cea.fr.
[32] P.B. Klufová, A. Kříž, M. Vostřák, Development of laser clads with high corrosion resistance for nuclear power industry, in: AIP Conference Proceedings, vol 2189, American Institute of Physics Inc., Pilsen, Czech Republic, 2019 020011, https://doi.org/10.1063/1.5138623, 2189.
[33] V.K. Sampath, P. Silori, P. Paradkar, S. Niauzorau, A. Sharstniou, A. Hasib, et al., 3d printing of stainless steel 316L and its weldability for corrosive environments, Mater. Sci. Eng. 833 (2022), https://doi.org/10.1016/j.msea.2021.142439.
[34] F. Sing, B. Ren, Cold spray additive manufacturing for new pipeline fabrication in live, natural gas distribution mains. https://doi.org/10.2172/2532395, 2022.
[35] T. Torims, F. Brückner, A. Ratkus, Additive manufacturing in-situ repair solutions for the FCC, Ann. Meet. Future Circular Collider Study (2018).
[36] C. Lamb, L. Thomson, J. Woodwark, S. Craig, I. Merrigan, T. Mindham, et al., Pipe maintenance tooling development for the ITER divertor remote handling system, Fusion Eng. Des. 136 (2018) 983–987, https://doi.org/10.1016/j.fusengdes.2018.04.051.
[37] K. Akowua, L. Aucott, D. Waillis, H. Raphael, C. Remi, B. Emmanuel, et al., Review and down-selection of NDE technologies suitable for ITER cooling water system remote weld inspections, Fusion Eng. Des. 196 (2023), https://doi.org/10.1016/j.fusengdes.2023.113980.
[38] L. Thomson, J. Woodwark, C. Kennedy, A. Muir, V. Agudo, I. Merrigan, et al., Neutral beam remote cutting & welding development, Fusion Eng. Des. 124 (2017) 487–491, https://doi.org/10.1016/j.fusengdes.2017.04.078.
[39] J.T. Pacheco, V.H. Meura, P.R.A. Bloemer, M.T. Veiga, O.C. de Moura Filho, A. Cunha, et al., Laser directed energy deposition of AISI 316L stainless steel: the effect of build direction on mechanical properties in as-built and heat-treated conditions, Adv.Industrial Manufact. Eng. 4 (2022), https://doi.org/10.1016/j.aime.2022.100079.
[40] G. Piscopo, L. Iuliano, Evaluating the effect of deposition strategy on mechanical characteristics of 316L parts produced by laser powder directed energy deposition process, Laser. Manufact. Mater. Process. 11 (2024) 419–436, https://doi.org/10.1007/s40516-024-00251-y.
[41] X. Zou, Z. Yan, K. Zou, W. Liu, L. Song, S. Li, et al., Grain refinement by dynamic recrystallization during laser direct energy deposition of 316L stainless steel under thermal cycles, J. Manuf. Process. 76 (2022) 646–655, https://doi.org/10.1016/j.jmapro.2022.01.057.
[42] A. Mithal, N. Maharjan, S. Idapalapati, Microstructural evolution in laser-based directed energy deposition of 316 L stainless steel with interlayer deformation, Mater. Char. 209 (2024), https://doi.org/10.1016/j.matchar.2024.113779.
[43] M. Elsayed, M. Khedr, A. Järvenpää, A.M. Gaafer, A. Hamada, Microstructure and hardness properties of additively manufactured AISI 316L welded by tungsten inert gas and laser welding techniques, Materials 17 (2024) 4489, https://doi.org/10.3390/ma17184489.
[44] M. Mokhtari, P. Pommier, Y. Balcaen, J. Alexis, Laser welding of AISI 316L stainless steel produced by additive manufacturing or by conventional processes, J. Manufact. Mater. Process. 5 (2021), https://doi.org/10.3390/jmmp5040136.
[45] H. Selmi, J. Brousseau, G. Caron-Guillemette, S. Goulet, J. Desjardins, C. Belzile, Weldability of 316L parts produced by metal additive manufacturing, J. Manufact. Mater. Process. 7 (2023), https://doi.org/10.3390/jmmp7020071.
[46] Y. Zhang, T. Yu, R. Xu, J. Thorborg, W. Liu, J. Tischler, et al., Local residual stresses and microstructure within recrystallizing grains in iron, Mater. Char. 191 (2022), https://doi.org/10.1016/j.matchar.2022.112113.
[47] K.K. Alaneme, E.A. Okotete, Recrystallization mechanisms and microstructure development in emerging metallic materials: a review, J. Sci. Adv. Mater. Devices 4 (2019) 19–33, https://doi.org/10.1016/j.jsamd.2018.12.007.
[48] X. Hu, H.Y. Jiang, Y. Luo, Q. Jin, W. Peng, C.M. Yi, A study on microstructure, residual stresses and stress corrosion cracking of repair welding on 304 stainless steel: part II-Effects of reinforcement height, Materials 13 (2020), https://doi.org/10.3390/ma13112434.
[49] M. Zhang, Z. Zhang, L. Lei, W. Zhou, M. Du, B. Zhang, Effect of repair weld length on microstructure evolution and mechanical properties of 30CrMnSiNi2A ultra-high strength steel, J. Mater. Res. Technol. 23 (2023) 4828–4842, https://doi.org/10.1016/j.jmrt.2023.01.175.
[50] P.L. Ferrandini, C.T. Rios, A.T. Dutra, M.A. Jaime, P.R. Mei, R. Caram, Solute segregation and microstructure of directionally solidified austenitic stainless steel, Mater. Sci. Eng., A 435–436 (2006) 139–144, https://doi.org/10.1016/j.msea.2006.07.024.
[51] T. Mukherjee, J.S. Zuback, A. De, T. DebRoy, Printability of alloys for additive manufacturing, Sci. Rep. 6 (2016) 19717, https://doi.org/10.1038/srep19717.
[52] P. Murkute, S. Pasebani, O. Burkan Isgor, Metallurgical and electrochemical properties of super duplex stainless steel clads on low carbon steel substrate produced with laser powder bed fusion, Sci. Rep. 10 (2020) 10162, https://doi.org/10.1038/s41598-020-67249-2.
[53] A. Kisielewicz, E. Sadeghi, F. Sikström, A.K. Christiansson, G. Palumbo, A. Ancona, In-process spectroscopic detection of chromium loss during directed energy deposition of alloy 718, Mater. Des. 186 (2020), https://doi.org/10.1016/j.matdes.2019.108317.
[54] P.A.A. Khan, T. Debroy, Alloying element vaporization and weld pool temperature during laser welding of AlSl 202 stainless steel, Metall. Trans. A B 15B (1984) 641–644, https://doi.org/10.1007/BF02657284.
[55] S. Kožuh, M. Gojićgojić, L. Vrsalovićvrsalović, Corrosion failure and microstructure analysis of AISI 316L stainless steels for ship pipeline before and after welding, Met. Mater. 51 (2013) 53–61, https://doi.org/10.4149/km_2013_1_53.
[56] B. Yelamasetti, G. Rajyalakshmi, Effect of TIG, pulsed TIG and interpulse TIG welding techniques on weld strength of dissimilar joints between monel 400 and AISI 316, in: Mater Today Proc, vol. 19, Elsevier Ltd, 2019, pp. 755–760, https://doi.org/10.1016/j.matpr.2019.08.125.